AGU PUBLICATIONS

JGR

Journal of Geophysical Research: Atmospheres

RESEARCH ARTICLE
10.1002/2014JD023008

Key Points:
- Beijing's urban extent, in terms of physical infrastructure change, quadrupled between 2000 and 2009
- Beijing's expansion created a ring of impact in the new portion of the city
- Urbanization slowed winds and increased pollution vertical dilution, temperature, and ozone

Correspondence to:
M. Z. Jacobson,
jacobson@stanford.edu

Citation:
Jacobson, M. Z., S. V. Nghiem, A. Sorichetta, and N. Whitney (2015), Ring of impact from the mega-urbanization of Beijing between 2000 and 2009, *J. Geophys. Res. Atmos.*, *120*, doi:10.1002/2014JD023008.

Received 22 DEC 2014
Accepted 19 MAY 2015
Accepted article online 21 MAY 2015

Ring of impact from the mega-urbanization of Beijing between 2000 and 2009

Mark Z. Jacobson[1], Son V. Nghiem[2], Alessandro Sorichetta[3,4], and Natasha Whitney[1]

[1]Department of Civil and Environmental Engineering, Stanford University, Stanford, California, USA, [2]Jet Propulsion Laboratory, California Institute of Technology, Pasadena, California, USA, [3]Geography and Environment, University of Southampton, Southampton, UK, [4]Institute for Life Sciences, University of Southampton, Southampton, UK

Abstract The transient climate, soil, and air quality impacts of the rapid urbanization of Beijing between 2000 and 2009 are investigated with three-dimensional computer model simulations. The simulations integrate a new satellite data set for urban extent and a geolocated crowd-sourced data set for road surface area and consider differences only in urban land cover and its physical properties. The simulations account for changes in meteorologically driven natural emissions but do not include changes in anthropogenic emissions resulting from urbanization and road network variations. The astounding urbanization, which quadrupled Beijing urban extent between 2000 and 2009 in terms of physical infrastructure change, created a *ring of impact* that decreased surface albedo, increased ground and near-surface air temperatures, increased vertical turbulent kinetic energy, and decreased the near-surface relative humidity and wind speed. The meteorological changes alone decreased near-surface particulate matter, nitrogen oxides (NO_x), and many other chemicals due to vertical dilution but increased near-surface ozone due to the higher temperature and lower NO. Vertical dilution and wind stagnation increased elevated pollution layers and column aerosol extinction. In sum, the ring of impact around Beijing may have increased urban heating, dried soil, mixed pollutants vertically, aggravated air stagnation, and increased near-surface oxidant pollution even before accounting for changes in anthropogenic emissions.

1. Introduction

This study examines the local transient climate, soil, and air quality response to the extreme decadal radial expansion of Beijing's urban infrastructure. Such impacts are determined after estimating the urban extent of Beijing from a new satellite data set and Beijing's total road area from a geolocated crowd-sourced data set. Both data sets are incorporated into the Gas, Aerosol, Transport, Radiation, General Circulation, Mesoscale, and Ocean Model (GATOR-GCMOM), which is a global-through-urban nested climate-weather-air pollution model [*Jacobson*, 2001a, 2001b, 2010, 2012; *Jacobson et al.*, 2007; *Jacobson and Ten Hoeve*, 2012], to simulate the effects of mega-urbanization of Beijing in the 2000s.

Previous data and results of modeling studies have been used to examine the effects of urbanization on urban temperatures [e.g., *Howard*, 1833; *Oke*, 1982; *Jones et al.*, 1990; *Peterson*, 2003; *Velazquez-Lozada et al.*, 2005; *Sarrat et al.*, 2006; *Oleson et al.*, 2011; *Jacobson and Ten Hoeve*, 2012]. The urban heat island (UHI) effect occurs because urban surfaces reduce evapotranspiration and have sufficiently different heat capacities, thermal conductivities, albedos, and emissivities to enhance urban warming. Some studies have examined the impacts of Beijing itself on precipitation and heat fluxes [e.g., *Zhang et al.*, 2009; *Wang et al.*, 2012a; *Yang et al.*, 2014; *Song et al.*, 2014; *Kuang et al.*, 2015]. Others have examined UHI impacts on air pollution in different locations [e.g., *Sarrat et al.*, 2006; *Jacobson and Ten Hoeve*, 2012].

This study examines the difference in both meteorological and air quality parameters arising from the new expansion of Beijing between 2000 and 2009. New advances are made by incorporating fairly precise data for the change in urban extent delineated based on physical infrastructures and for the locations and sizes of roads in the megacity. Locating and sizing roads are important because roads have properties that are different from rooftops and vegetation, which are distinctively treated in GATOR-GCMOM.

2. Integration of Urban Extent From Satellite Observations

In the decade of the 2000s, worldwide urbanization occurred at an astounding rate, particularly in Asia, with the extensive expansion of multiple megacities [*United Nations, Department of Economic and Social Affairs*,

Population Division, 2014]. Among them, Beijing is undergoing the most transformative change [*World Bank and the Development Research Center of the State Council, P. R. China*, 2014]. An understanding of urban change becomes imperative as the world urbanizes. Rapid and haphazard urban development may disproportionally impact the environment both locally and perhaps well beyond urban areas.

Understanding the impacts of infrastructure change on the environment requires first a quantification of the infrastructure change itself. Major information gaps still exist in quantifying key parameters, such as urban extent, residential area, and commercial/industrial core area, relevant to infrastructure change. Despite an array of urban reports and publications, urban extent is defined differently and arbitrarily within and among countries based on local administrative, political, or legislative decisions. Many definitions are nonphysical and inapplicable to physically based three-dimensional climate-air quality models, which require a true representation of physical urban infrastructure.

One method of quantifying urban extent is from optical or multispectral satellite remote sensing. Although urban areas or other human settlements, in general, can readily be observed visually, an accurate and consistent quantification with spectral remote sensing has proven elusive [*Li et al*., 2014]. While spectral-mixing approaches have advanced certain representations of urban land [*Kressler and Steinnocher*, 1996; *Small*, 2005; *Zhang et al*., 2013], the spectral similarity among many impervious surfaces and pervious soils remains a fundamental difficulty [*Weng et al*., 2009], causing inconsistent estimations of urban extent.

For example, Beijing urban extent estimated from Landsat data is ~1035 km^2 by *Xie et al*. [2007] but ~2232 km^2 by *He et al*. [2006]. The difference of more than a factor of 2 is due in part to He et al.'s misclassification of a pervious dirt area in a quarry in Fangshan as an impervious cement color urban sector [*Sorichetta et al*., 2014]. The overestimation of the Beijing extent by *He et al*. [2006] significantly underestimates the rate of Beijing change. Similarly, the definition and calculation of a so-called urban "built-up" area in a city differs widely among studies [*Zhang et al*., 2009; *Wang et al*., 2012b].

In order to overcome the issue of inconsistent and arbitrary definitions or estimations of city boundaries, we need to develop a spatially and temporally consistent urban extent data set to delineate and characterize physical infrastructures and changes in urban and suburban environments consistently in time and in space. Satellite data with both high resolution and large coverage are needed in this endeavor to minimize spatial and temporal gaps. These requirements for satellite data pose a critical challenge because high-resolution data suffer from small and sporadic coverage in time and space inconsistently collected by different investigators whereas large-coverage wide-swath satellite data suffer from very low resolution thus are insufficient to study urban and suburban environments.

Here we use an innovative method to estimate urban extent and monitor urban changes over time: the dense sampling method (DSM) based on the invention of the Rosette Transform (RT) [*Nghiem et al*., 2009]. The RT operates on radar backscatter (σ_0) data, acquired globally during the decade of the 2000s with the SeaWinds scatterometer (a stable and accurate radar) aboard the QuikSCAT satellite [*QuikSCAT Mission*, 2014]. Radar backscatter data represent urban observations on the basis of physical infrastructures (houses, buildings, factories, shopping centers, skyscrapers, freeway networks, etc.). This is because radar backscatter depends on the number of, size of, and materials within buildings (e.g., higher backscatter for more buildings, for larger and taller buildings, and for stronger materials like steel).

In DSM, the radar equation is first cast in a mathematical formulation similar to the Radon Transform. Nevertheless, unlike the Radon Transform used in medical imaging (requiring a patient to be kept strictly unchanged under a strong power source) for which Hounsfield and Cormack earned the 1979 Nobel Prize, the new RT can account for variability in the natural environments as well as in man-made urban areas (e.g., azimuth change in different sides of buildings and vehicle traffics) and for weak power from a remote satellite in Earth orbit. The accuracy of the new method has been tested over Príncipe Island [*Nghiem et al*., 2009].

Within the framework of DSM, we make an ensemble average of N samples of backscatter data measured at azimuth angle ϕ_i at time t_i densely populated within area A from many measurements with their footprint centers collocated at (x_k, y_k) to form a σ_0 ensemble for all azimuths over a given time period (e.g., a year). The σ_0 ensemble is decomposed into a mean part and a zero-mean fluctuating part. In this process, the RT is applied to derive high-resolution data in space at the expense of the temporal resolution. There are two

terms obtained from DSM: a mean value representing the average over an annual period and an index of variability (IV) characterizing the variations around the mean.

In an urban area, the mean term from DSM is typically higher than that in surrounding rural areas. However, some natural targets may also have a high mean σ_0 (e.g., land with a thick snow cover). Thus, the mean by itself is not sufficient to identify uniquely urban areas. This is where the use of IV becomes necessary for urban detection: IV is also typically high in an urban environment due to the large backscatter variability associated with human-made targets (e.g., different sides of buildings, orientation of building corners, and vehicle traffic). Combining both the mean and IV, we have successfully applied the DSM for urban remote sensing to delineate and map urban extent and typology for various cities in the U.S., Colombia, Bangladesh, China, and Ecuador [*Nghiem et al*., 2009, 2014].

Here DSM is used with satellite scatterometer backscatter data to delineate Beijing urban extent as well as interurban and intraurban changes at a posting scale of 0.008333° (about 1 km at the equator) from 2000 to 2009. The DSM-RT technique enables the use of scatterometer data at a resolution sufficient for monitoring annual and interannual urban changes by combining dense data samples collected from daily observations. Moreover, the DSM-RT technique, used to increase the resolution of the scatterometer data, breaks through the limitation of the traditional deconvolution method that is invalid in urban environments due to azimuth anisotropic changes (presence of nonspherical buildings, alignment of city blocks, road networks, etc.) and due to transient or episodic changes over cities (vehicle traffic, rain, snow, etc.).

Previously, QuikSCAT/DSM-RT data were used to study the spatial pattern of Beijing, revealing a strong association between the presence of building infrastructures and daily averaged ambient population [*Nghiem et al*., 2014]. Ambient population data are taken from the LandScan^{TM} data set (LandScan 2008^{TM}/ UT-Battelle, LLC) representing the average number of people living and working in buildings [*Dobson et al*., 2000] rather than the number of people allocated in artificial administrative units where they have their addresses registered (i.e., residential population). With the linear correlation analysis from 5% random sampling of the large number of DSM raster grid cells, a relationship between QuikSCAT/DSM-RT observations and the ambient population is found with a Pearson's correlation coefficient as high as 0.724 [*Nghiem et al*., 2014].

Rather than relying on just a static representation of the Beijing built pattern, this study first processes QuikSCAT data using DSM-RT each year between 2000 and 2009 to monitor the trend in Beijing urbanization during that period. Urbanized pixels are defined here as those with DSM σ_0 larger than -8 dB and DSM IV larger than 2 dB. These values, used to estimate the urban extent of Beijing each year, are determined from a training data set based on the city of Wuhan in China as a test city for calibration and validation. Since Wuhan is a different city from Beijing, testing with it avoids the self-validation issue. Figure 1 shows the resulting Beijing urban extents for 2000 and 2009 along with the city boundaries. In some pixels in inner Beijing, noise from satellite data arises, and an isolated pixel-wise estimate of change (equivalent to taking the derivative) can result in a nonlinear noise amplification. It is cautioned against interpreting the noise. It is better to consider the robust linear regression over the whole decadal data set [*Stevenazzi et al*., 2015].

Figure 1 indicates that the urban extent within the Beijing Municipality, calculated with QuikSCAT/DSM-RT data and the ASPHAA algorithm for computing cell area [*Santini et al*., 2010], almost quadrupled between 2000 and 2009, from 1105 km^2 to 4139 km^2. These results compare to within 6% of an independent estimate (1035 km^2) from Landsat data for the year 2000 [*Xie et al*., 2007] and to within 8% of the official urban extent (4480 km^2) taken for the year 2009 [*Wikipedia*, 2014]. The remaining 12,239.9 km^2 of the administrative Beijing Municipality consists of rural areas, nature reserves, and lightly populated mountains [*Wikipedia*, 2014] so that the total of 4480 km^2 + 12,239.9 km^2 = 16,719.9 km^2 should not be considered the true urban extent of Beijing, which is the part of Beijing that actually has physical infrastructures such as houses, buildings, factories, shopping centers, skyscrapers, and freeways, which are important and relevant to the physically based modeling with GATOR-GCMOM.

3. Integration of Total Road Surface Area From Geolocated Crowd-Sourced Data

The GATOR-GCMOM model used for this study treats roads, rooftops, and vegetated and bare soil surfaces at the subgrid scale [*Jacobson*, 2001a]. Land cover in the model outside of Beijing is determined at 0.01°

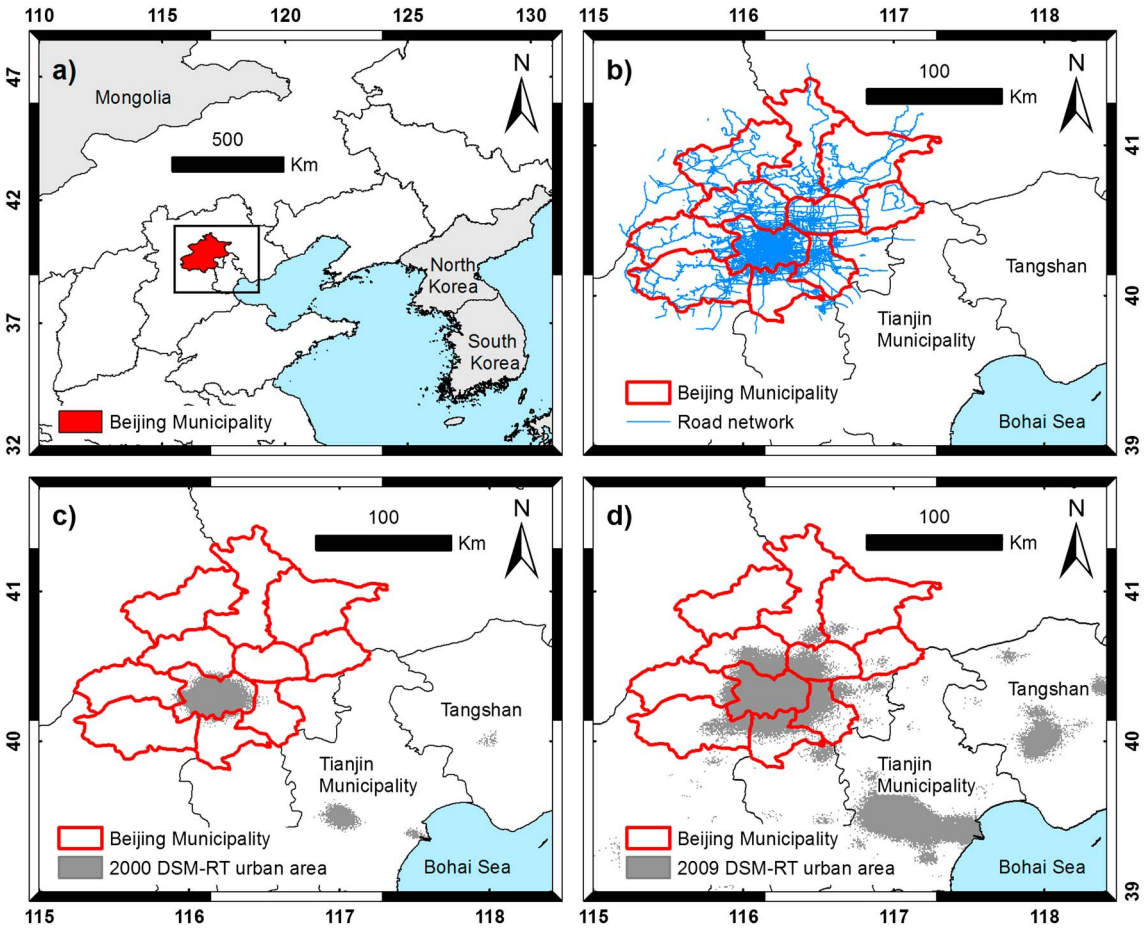

Figure 1. (a) Beijing Municipality (Beijing city proper, Beijing districts, and Beijing counties combined) in the context of East Asia. (b) Network of roads within the Beijing Municipality in 2013 from OSM data. The total road area is 279 km^2 (Table 1). The red lines demark Beijing administrative units (city proper, districts, and counties). (c) Beijing urban extent in 2000 as determined from QuikSCAT/DSM-RT data. The total area in the Beijing Municipality is 1105 km^2. This area does not include the areas in the Tianjin and Tangshan Municipalities. (d) Same as Figure 1c but for 2009. The total area in the Beijing Municipality is 4139 km^2.

resolutions from *United States Geological Survey* (*USGS*) [2006] data. Such data include urban and buildup land, agricultural land, and many types of natural lands. Here we superimpose QuikSCAT/DSM-RT urban extent data onto the *USGS* [2006] data. However, urban extent data do not give a breakdown of how urban areas are divided into roads, rooftops, vegetation cover, and bare soil. Previous modeling studies have either ignored the partitioning or approximated the division as constant throughout an urban region based on a few sparse measurements in different parts of the world. However, a more realistic and spatial division is desired because the properties of each surface type in an urban area differ. Here we approximate road areas in the Beijing urban extent with a novel approach in an effort to improve the calculation. We hypothesize but do not prove that the inclusion of more accurate road data improves the accuracy of the overall calculation.

Thus, the next step in this study is to determine the total road surface area in each pixel of the Beijing QuikSCAT/DSM-RT urban extent data set at a pixel size of 0.008333°. To accomplish this, we use OpenStreetMap (OSM) road data. The worldwide diffusion of the Internet along with the development of Web 2.0 technology during the 2000s together with the more recent widespread use of GPS-enabled portable devices have empowered people to collect geographic information and readily contribute it to the Web as volunteered geographic information (VGI) [*Goodchild*, 2007]. This information is usually made available to end users through online platforms and represent the only source of geographic information for places where official and commercial geographic information is either difficult to obtain, not accessible, or not available [*Goodchild*, 2007].

One of the most used and analyzed VGI platforms derived from crowd-sourced data is OSM [*Neis and Zielstra*, 2014]. The OSM project started in 2004 and has the long-term objective of creating a free open-access database of worldwide geographic information entirely contributed on a voluntary basis (OpenStreetMap, 2014, http://www.openstreetmap.org).

OSM vector road data, obtained primarily from GPS-enabled portable devices, satellite images, and commercial and governmental data sets that comply with the project license can be contributed only by registered members and are not reviewed before being made public on the Internet [*Neis and Zielstra*, 2014]. The fact that OSM data are not reviewed before being distributed is largely perceived as one of the main added values of the project [*Neis et al*., 2012a] but also raises concern about OSM data quality and reliability [*Flanagin and Metzger*, 2008].

A number of studies have assessed the quality of OSM road data focusing on Europe, the United States, and China [*Haklay*, 2010; *Girres and Touya*, 2010; *Zielstra and Zipf*, 2010; *Zielstra and Hochmair*, 2011; *Koukoletsos et al*., 2012; *Neis et al*., 2012b; *Zielstra et al*., 2013; *Wang et al*., 2013; *Will*, 2014; *Zheng and Zheng*, 2014]. Different methods have been used to compare geometrical accuracy, positional accuracy, and completeness [*International Organization for Standardization*, 2013] of OSM road data with respect to either official or commercial road data sets. Results consistently indicate that both accuracy and completeness, although spatially heterogeneous, are generally good. Furthermore, OSM data completeness increases over time and is commonly greater in built environments, where OSM data can be considered a valid alternative to official and commercial data [*Song and Sun*, 2010]. In particular, OSM road data are mostly complete, with accuracy $>$70%, in Beijing [*Zheng and Zheng*, 2014].

OSM data are distributed under the Open Data Commons Open Database License (Open Data Commons, 2014, http://opendatacommons.org/licenses/odbl/) and can be either downloaded from the OSM website or retrieved from other sources including, for example, Geofabrik's OSM Data Extracts [http://download.geofabrik.de/] and BBBike.org [http://extract.bbbike.org/].

The Beijing OSM road data set used for this study was downloaded from CloudMade.com (http://downloads.cloudmade.com) on 10 September 2013 and contains 29 types of roads that extend for a total length of about 14,946 km (http://wiki.openstreetmap.org/wiki/Key:highway provides a detailed description of the road types, which are listed in Table 1).

The total road surface within each pixel of the Beijing QuikSCAT/DSM-RT data set in 2000 and 2009 is estimated as follows. First, after reprojecting the road vector data from Geographic Coordinate System (GCS) World Geodetic System (WGS) 84 to WGS 84/Universal Transverse Mercator (UTM) Zone 50N in a Geographic Information System environment, we calculate the total length of each road type in each pixel. To calculate road widths, we first randomly select 10 samples for each road type available in the Beijing OSM data set and then use optical high-resolution images (Google Earth Pro 7.1.2.2041, 2013, http://www.google.com/work/mapsearth/products/earthpro.html) to estimate the mean width and associated standard error of each road type (the latter ranging between 0 and 5 m; Table 1). Finally, we multiply the mean width of each road type by the corresponding total road length in each pixel to obtain the surface area of each road type in each pixel, the sum of which represents the total road surface area in each pixel.

The total road surface area for Beijing is estimated using the OSM road data set downloaded on 10 September 2013. Indeed, even if the full history of the OSM database were downloaded (http://planet.openstreetmap.org/planet/full-history/), it would not be possible, at a given point in history, to distinguish between roads that were not yet contributed to the database and roads that had not yet been built. Thus, we conservatively use the most recent version of the OSM road data set available at the commencement of this study. We overlay the 2013 road surface areas onto the Beijing QuikSCAT/DSM-RT urban extents determined for 2000 and 2009 to calculate the Beijing road areas in 2000 and 2009, respectively. This approach accounts for new roads in newly developed expansion of Beijing while maintaining the same road fraction with the urban extent common to both the years 2000 and 2009. While this approach is consistent with the fact that most roads already existed in the sector common to 2000 and 2009 and more new roads could be built in the new sector by 2009, it cannot account for new roads in the old sector. The approach also does not account for roads in the new sector that may have existed in 2000 within nonurban land cover pixels since *USGS* [2006] does not account for roads in nonurban land cover pixels.

Table 1. Mean Road Widths and Standard Errors for Each OSM Road Type in Beijing Calculated Using the Method Described in the Text[a]

Class	Road Type	Total Length (km) 2013	Mean Width (m)	Standard Error (m)	Total Area (km^2) 2013
1	Bridleway	1.6	15.28	0.62	0.02
2	Bus guideway	5.3	11.31	0.38	0.06
3	Construction	13.8	10.23	1.3	0.14
4	Crossing	0.05	7.76	0.16	0.0004
5	Cycleway	46.9	5.12	0.94	0.24
6	Escape lane	0.6	11.54	1.32	0.01
7	Footway	328.6	2.32	0.35	0.76
8	Living street	7.3	7.18	1.37	0.05
9	Motorway	1,680.7	28.7	2.61	48.24
10	Motorway link	381.8	10.33	0.87	3.94
11	No type	0.8	8	0	0.01
12	Path	95.7	2.14	0.23	0.20
13	Pedestrian	18.7	9.09	1.95	0.17
14	Platform	8.9	4.48	0.4	0.04
15	Primary	1,252.1	24.49	5.05	30.67
16	Primary link	21.3	13.93	1.17	0.30
17	Residential	2,133.2	12.18	1.72	25.98
18	Road	266.6	10.83	1.6	2.89
19	Secondary	2,575.8	27.42	4.19	70.63
20	Secondary link	24.5	9.55	0.65	0.23
21	Service	427.0	9.95	1.8	4.25
22	Steps	6.3	4.07	0.78	0.03
23	Tertiary	3,812.6	17.92	1.46	68.32
24	Tertiary link	20.3	20.54	4.49	0.42
25	Track	94.3	4.21	0.81	0.40
26	Traffic Signals	0.0	21.2	0.24	0.0003
27	Trunk	513.1	23.09	2.7	11.85
28	Trunk link	163.7	6.35	0.8	1.04
29	Unclassified	1,044.3	7.98	1.14	8.33
	Total or mean	14,945.7	18.68	2.37	279.21

[a]Data are valid for 2013.

The total road surface area in each pixel determined from the OSM road data set is interpolated into each GATOR-GCMOM model grid cell. The road surface area in a model grid cell divided by the cell area is the road fraction in the cell. The maximum road fraction, which is within the Beijing city center, is ~29%. The 2013 total road surface area calculated for Beijing is 279 km^2 (Figure 1 and Table 1), which represents ~6.7% of the total Beijing urban extent in 2009. Figure 1 indicates that the main roads emanate radially from the city center with increasing-circumference circular rings occurring with increasing distance from the center. The approach for road fraction estimation accounts for the radial expansion of Beijing, where the new ring roads are built around and outward from the old Beijing center.

The total road surface area in each grid cell is then subtracted from the total urbanized area in the same grid cell, determined from the QuikSCAT/DSM-RT urban extent data set, to obtain the nonroad urban area assumed to be covered by rooftops in each cell. The nonurbanized area of each model grid cell is further assumed to consist of both bare and vegetated soil, with the vegetation fraction derived from Moderate Resolution Imaging Spectroradiometer (MODIS) Normalized Difference Vegetation Index (NDVI) data as in *Jacobson and Ten Hoeve* [2012]. In regions of the model domain where OSM road data are not available or QuikSCAT/DSM-RT urban pixels are not detectable (e.g., small and isolated human settlements), *USGS* [2006] global land use data at 0.01° resolution are used to determine land surface type. Pixels classified as urban and built-up pixels in this data set, which are in more rural areas and cities outside of Beijing, are then broken into rooftop, road, bare soil, and vegetated soil data as in *Jacobson and Ten Hoeve* [2012].

4. Description of the GATOR-GCMOM Model

This section describes the remaining processes treated in the GATOR-GCMOM model. The model treats interactive feedback among gas, aerosol, radiative, meteorological, cloud, and ground surfaces, and ocean

processes without data assimilation or nudging and with an interactive ocean. The model has been evaluated against paired-in-time-and-space or paired-in-space gas, aerosol, meteorological, and/or radiative data in several studies [e.g., *Jacobson*, 2001a, 2001b, 2010; *Jacobson et al.*, 2007; *Jacobson and Streets*, 2009].

4.1. Meteorological, Transport, Gas, and Surface Processes

The momentum equation is solved with the potential enstrophy, vorticity, energy, and mass-conserving scheme of *Arakawa and Lamb* [1981] on the global scale and with the enstrophy-conserving, mass-conserving, and kinetic-energy-conserving scheme of *Lu and Turco* [1995] on regional scales. Two-dimensional ocean mixed-layer dynamics conserve potential enstrophy, vorticity, energy, and mass while providing mixed-layer velocities, heights, and energy transport [*Ketefian and Jacobson*, 2009]. The model solves 3-D ocean energy and chemistry diffusion, 3-D ocean equilibrium chemistry, and ocean-atmosphere exchange with mass-conserving and unconditionally stable schemes among 10 ocean layers [*Jacobson*, 2005b]. The top ocean layer thickness for dynamics, diffusion, and chemistry is calculated with the 2-D ocean dynamics scheme.

Horizontal and vertical atmospheric advection of gases and size-resolved and composition-resolved aerosol particles are solved with the mass-conserving, peak-preserving, mixing ratio bounded scheme of *Walcek* [2000]. Eddy diffusion coefficients, used in a second-order local closure gas and particle diffusion scheme, are calculated with the *Mellor and Yamada* [1982] level 2.5 parameterization. Gas processes include emissions, photochemistry, gas-to-particle conversion, gas-to-cloud conversion, gas-cloud exchange, gas-ocean exchange, advection, convection, molecular diffusion, turbulent diffusion, and dry deposition. Gas photochemistry is solved with sparse-matrix vectorized Gear solver version II (SMVGEAR II) for over 400 tropospheric and stratospheric kinetic, heterogeneous, and photolysis reactions.

In each model land surface grid cell, the model treats water and energy transport through 10 subsurface soil layers for each of up to 13 subgrid soil types. It also treats energy transfer through roads overlying soil, vegetation, and snow over soil; multiple layers of rooftop material over air; and water bodies, including those covered with sea ice and snow on sea ice [*Jacobson*, 2001a; *Jacobson and Ten Hoeve*, 2012]. The model further solves for the depth, aging, compaction, and horizontal transport of sea ice, conserving mass [*Jacobson*, 2012]. Sea ice velocities are a function of surface wind velocity, ocean velocity, the Coriolis parameter, and drag coefficients between the air and sea ice and sea ice and water [e.g., *Nakayama et al.*, 2012] and are solved for with a Newton-Raphson iteration.

Roads are assumed to consist of 5 cm thick asphalt, impermeable to water and with asphalt properties, overlying soil. In terms of the 10-layer subsurface module, the top five layers are treated as asphalt, and the rest are treated as a soil-air-water mixture. Snow and liquid water can accumulate on the asphalt as an additional (eleventh) layer in the subsurface module. Roofs are assumed to consist of five layers of roofing material on top of five air layers [*Jacobson*, 2001a; *Jacobson and Ten Hoeve*, 2012]. Dew that collects on the roof can evaporate.

During each subsurface module time step (15 s), surface and subsurface temperatures and moisture, sensible heat fluxes, latent heat fluxes, water vapor fluxes, friction wind speeds, Monin-Obhukov lengths, Richardson numbers, snow depths, ice thicknesses, sublimation rates, runoff, foliage temperatures, leaf stomata specific humidities, foliage air temperatures, foliage specific humidities, and water/snow stored on leaves, roads, and roofs are calculated for each surface class in each grid cell from the column subsurface module. Surface temperatures, sensible heat fluxes, latent heat fluxes, and water vapor fluxes are then weighted by the fractional surface type in the cell to give an effective value for the whole cell. *Jacobson* [2001a, Figure 3, 2001b, Figure 3] compare modeled temperatures from this method with hourly data over 4 days at two dozen locations, including in cities.

The surface albedo of each grid cell at each wavelength is the area-weighted sum of the albedos of each surface class in the cell. The albedos of roads and roofs are assumed to be those of asphalt. Solar albedos of paved asphalt range from 0.04 (new) to 0.17 (aged), averaging 0.12 [*Pon*, 1999]. Albedos of all other surfaces are from 0.05° MODIS combined Terra plus Aqua satellite data in seven spectral bands [*Moderate Resolution Imaging Spectroradiometer/USGS*, 2007; *Schaaf et al.*, 2002]. These solar albedos are interpolated spatially and spectrally to each of 86 solar wavelengths below 800 nm and 232 solar-IR wavelengths/probability intervals from 800 to 5000 nm.

4.2. Aerosol Processes

Aerosol processes include anthropogenic and natural emissions, binary and ternary homogeneous nucleation, condensation, dissolution, internal particle chemical equilibrium, aerosol-aerosol coagulation, aerosol-hydrometeor coagulation, sedimentation, dry deposition, and transport [*Jacobson*, 2002, 2003, 2012]. The model treats any number of discrete aerosol size distributions, each with any number of size bins and chemicals per bin. Particle number and mole concentrations of each chemical are tracked in each size bin. The components within each size bin of each aerosol size distribution are internally mixed in the bin but externally mixed from other bins and other size distributions. For this study, three aerosol size distributions, with 14 size bins per distribution, are used: an emitted fossil fuel soot distribution, an emitted biofuel and biomass burning soot distribution, and an ultimate internally mixed distribution. These distributions and their composition are described further in *Jacobson* [2012].

4.3. Convective Cloud, Stratiform Cloud, and Aerosol-Cloud Processes

The model treats first and second indirect aerosol effects on clouds explicitly and together with cloud absorption effects. For the two fine nested regional domains here (over China and Beijing) both cloud thermodynamics and microphysics are solved explicitly and at the grid scale [*Jacobson et al*., 2007]. For the global domain, convective clouds are treated at the subgrid scale, with multiple cloud clouds per column, and stratus clouds are treated at the grid scale. However, all cloud and precipitation microphysics are time dependent, explicit, size resolved, and composition resolved [*Jacobson*, 2003, 2012; *Jacobson et al*., 2007].

During cloud thermodynamics calculations, size-resolved and composition-resolved aerosols and gases are transported vertically in grid-scale and subgrid clouds for all model domains and horizontally in grid-scale clouds (high-resolution domains). Condensational and depositional growth/evaporation of water are solved simultaneously over all aerosol size distributions and simultaneously for liquid, ice, or both, in clouds on all scales.

The model treats three hydrometeor size distributions (liquid, ice, and graupel), each with 30 size bins (0.5 μm to 8 mm in diameter), and tracks concentrations of all aerosol component inclusions in each size bin of each hydrometeor distribution. *Jacobson* [2003, 2012] describes cloud and aerosol-cloud microphysical processes treated in detail.

4.4. Radiative Processes

For heating rate and photolysis calculations, each model column is divided into clear-sky and cloudy-sky columns, and separate calculations are performed for each. Radiative transfer is solved simultaneously through multiple layers of air and one snow, sea ice, or ocean water layer at the bottom to calculate, rather than prescribe, spectral albedos over these surfaces. Since the model tracks black carbon (BC), brown carbon (BrC), soil dust, and all other aerosol inclusions within precipitation particles that fall onto snow and sea ice, the radiative transfer calculation accounts for the optics of all these absorbing aerosol constituents within and between snow and sea ice grains [*Jacobson*, 2012] as well as within aerosol particles and within and between cloud and precipitation particles. Thus, the model explicitly treats both the microphysical and radiative effects of aerosols on clouds and precipitation. The optical properties of snow and sea ice containing absorbing cores are calculated from Mie scattering theory assuming an equivalent radius of snow or ice. The radius varies with the age of the snow/ice as a function of temperature and vertical temperature gradient [*Jacobson*, 2012].

The radiative transfer code used for heating rates and actinic fluxes [*Toon et al*., 1989] is solved for each of 694 wavelengths/probability intervals in each cloudy and clear portions of each model column with gas absorption coefficients from *Jacobson* [2005a]. In aerosol particles, black carbon for optical calculations is treated as a core surrounded by a mixed shell [*Ackerman and Toon*, 1981]. Ultraviolet and short-visible absorption by organic carbon and soil dust are also accounted for [*Jacobson*, 2012]. Since all aerosol component concentrations are tracked in each size of each hydrometeor particle type (liquid, ice, and graupel) throughout the evolution of clouds and precipitation, it is possible to calculate cloud absorption due to BC, BrC, and soil dust inclusions in clouds. For each size of a liquid, ice, or graupel particle, BC, BrC, and soil dust are treated as polydisperse spherules randomly spread throughout the hydrometeor particle [*Jacobson*, 2012]. The cloud particle's resulting optical properties are calculated with the iterative dynamic effective medium approximation [*Chylek et al*., 1984].

4.5. Emissions

The anthropogenic emission inventory used for this study is the Fifth Assessment Report inventory for 2005 assuming the Representative Concentration Pathway 4.5 trajectory [*Clarke et al.*, 2007]. This inventory is at 0.5° horizontal resolution. Emitted pollutants include CO, CH_4, acids, alcohols, benzene, butanes, chlorinated hydrocarbons, esters, ethane, ethene, ethers, ethyne, formaldehyde, hexanes and higher alkanes, ketones, other volatile organic compounds (VOCs), other alkanals, other alkenes, other aromatics, pentanes, propane, propene, terpenes, toluene, trimethylbenzenes, xylene, NO, NO_2, NH_3, SO_2, SO_3, BC, and primary organic carbon. For CO_2, N_2O, CFCs, and hydrofluorocarbons, the EDGAR 2005 inventory is used [*European Commission Joint Research Centre/Netherlands Environmental Assessment Agency*, *PBL*, 2014].

Open biomass burning and biofuel burning emissions, including components and time resolution, are described in *Jacobson* [2012]. Natural emissions from lightning (NO, NO_2, HONO, HNO_3, N_2O, H_2O_2, HO_2, and CO), soils (dust, bacteria, NO, N_2O, H_2, CH_4, H_2S, dimethylsulfide (DMS), carbonyl sulfide (OCS), and CS), oceans (bacteria, sea spray, DMS, N_2O, H_2, CH_4, and CH_3Cl), and vegetation (pollen, spores, isoprene, monoterpenes, methanol, and other VOCs) are calculated as a function of modeled meteorology as in *Jacobson and Streets* [2009].

For CO_2, the model treats chlorophyll photosynthesis in ocean and lake water; green plant photosynthesis over land; chlorophyll and leaf respiration; soil respiration; CO_2 dissolution in/evaporation from clouds, precipitation, and water bodies; weathering of silicate rocks; chemical production by atmospheric gases; ocean equilibrium chemistry; ocean formation of carbonate minerals; and CO_2 diffusive transport to the deep ocean, in addition to anthropogenic emissions [*Jacobson*, 2005b; *Jacobson and Streets*, 2009].

5. Simulations

Three global-through-local nested domains are used. The global domain has resolution 4° S-N × 5° W-E, with 68 sigma-pressure layers from the ground to 0.219 hPa (≈60 km), including 15 layers in the bottom 1 km and 500 m resolution from 1–21 km. A finer nested domain over China consists of 146 S-N and 156 W-E horizontal cells of resolution 0.33° and 0.45°, respectively, and a southeast corner at 15°N and 75°E. The finest domain over Beijing consists of 146 S-N and 156 W-E horizontal cells of resolution 0.015° and 0.025°, respectively, and a southeast corner at 38.815°N and 115.05°E. The regional domains include 55 layers from the surface to 47.3 hPa, matching exactly the bottom 55 sigma-pressure levels of the 68-layer global domain. Emissions enter all three domains, and all gas, aerosol, radiative, dynamical, and surface processes are solved in all domains. Gases and particles are transported from courser domains to finer domains, allowing for long-range transport of pollutants into finer domains.

Four simulations are run: two (for January and July) with 2009 Beijing urban, road, and roof fractions in each grid cell and the other two (for January and July) with 2000 fractions. Urban infrastructure changes accounted for are those in Figure 1 to the west of 118.2°E and to the north of 39.3°N. Meteorological fields are initialized with Global Forecast System 1° × 1° reanalysis fields on either 1 January or 1 July of an arbitrary common year, 2012 [*Global Forecast System*, 2013]. Each simulation is run for 1 month.

The only difference between the 2009 and 2000 simulations is the greater road and roof areas in 2009. All else, including the initial meteorology and emissions, is the same between the two simulations in order to isolate the impacts of infrastructure changes only.

When a roof or road land use type replaces a vegetated or unvegetated soil land use type in the model, several surface properties change as well. First, when a road replaces soil or vegetated soil, water can no longer evaporate from the soil below the road, but dew or rain can collect on the road and that water can evaporate. Similarly, soil water cannot evaporate when a building with a roof replaces soil or vegetated soil. Second, the heights; surface roughness lengths for momentum, heat, and moisture; albedos; emissivities; thermal conductivities; specific heats; and bulk densities of roads and roofs differ from those of vegetated or unvegetated soil in the model (section 3) [*Jacobson*, 2001a; *Jacobson and Ten Hoeve*, 2012].

6. Results

Figures 2–11 show 2009 minus 2000 average differences in several parameters for each January and July. Even within the short simulation period in each case, the impacts of urbanization in Beijing on

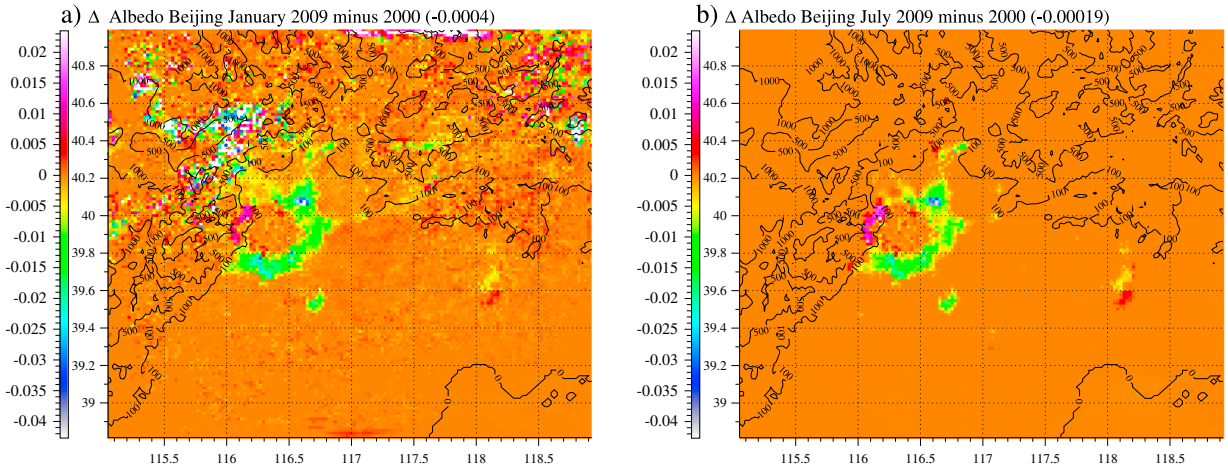

Figure 2. Simulated differences in Beijing surface albedo between 2009 and 2000, for each January and July in the innermost GATOR-GCMOM nested model domain. The black lines are topographical heights in meters. Differences in the model were calculated based on urban infrastructure changes in Figure 1 to the west of 118.2°E and to the north of 39.3°N.

atmospheric parameters are vivid. All figures indicate significant changes in a *ring of impact* corresponding to the Beijing urban expansion by new development since 2000. The sign of differences between 2009 and 2000 results is consistent for each January and July, but magnitudes vary for some parameters, as discussed shortly.

Urbanization decreases surface albedo (Figure 2) due to the darkness (lower albedo) of road and roof surfaces relative to vegetated surfaces that the urban areas replace. Urbanization similarly decreases soil moisture in the ring of impact (Figure 3) because impervious road and building surface inhibit the downward flux of water vapor and precipitation to the soil. The reduction in soil moisture due to urbanization is greater in July than in January because the absolute and relative humidities of near-surface air are greater in July than in January, so more air moisture is blocked from the soil by urban surfaces in July.

The reduction in soil moisture due to urbanization and lower water contents of roads and rooftops relative to soil increase the average soil-road-roof ground surface temperature during the day while decreasing it during the night. The net change is an increase in surface temperature in the ring of impact (Figure 4). For example, the domain-averaged ground surface temperature in July increased by ~0.3 K during daytime but decreased by ~0.15 K during the night. The nighttime cooling due to urbanization is due to the lower specific heat of urban surface than of soil containing water.

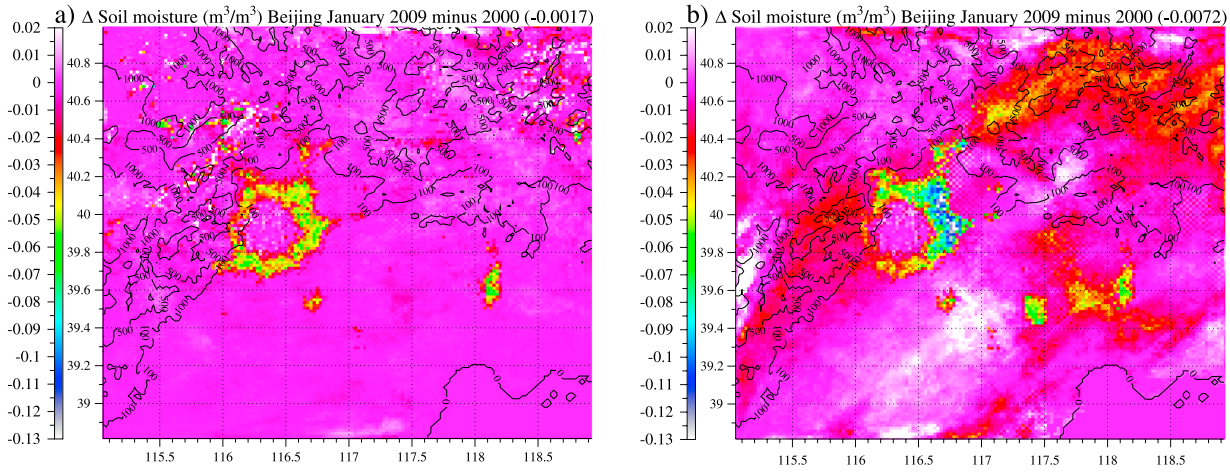

Figure 3. Same as Figure 2 but for soil moisture.

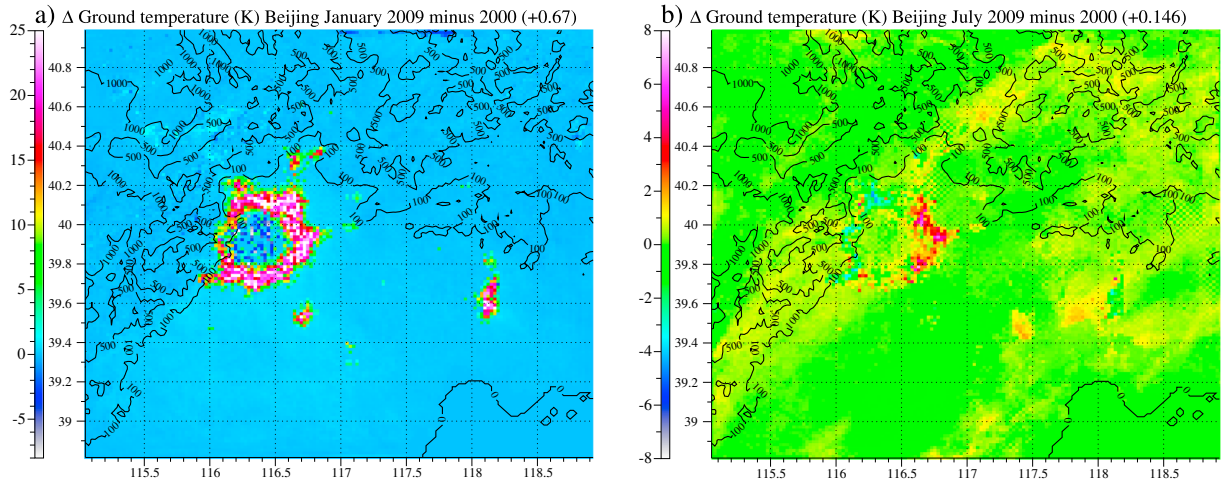

Figure 4. Same as Figure 2 but for ground temperature.

Due to their low moisture contents (thus lower specific heats and evaporation rates) and low albedos, road surfaces and roofs heat up to a greater extent during the day than do soil and vegetated surfaces. Evaporation is a cooling process, so low evaporation from roads and roofs warms the surface. The lower albedos of roads and roofs decrease net upward minus downward surface solar radiation, also increasing ground surface temperature during the day. However, the low specific heat of urban surfaces relative to soil causes urban surfaces to cool to a greater extent at night than do soil surfaces. The nighttime cooling is less than the daytime warming.

Ground temperatures increase more in January than in July. Background ground temperatures without urban surfaces are ~42 K lower in January than in July, preconditioning a large capacity to increase in January. When ground temperatures are low, conduction of heat from the deep soil easily escapes to the air, preventing the ground from holding the heat. However, the encapsulation of soil allows urban surfaces to absorb the conducted soil heat, contributing to the surface warming in January. Further, the absorption of sunlight and sensible heat by dry urban materials with low specific heat and albedo allows urban surface temperatures to rise further.

The increase in ground temperature translates into an increase in near-surface air temperature (Figure 5) upon urbanization. The summer increase in air temperature in Beijing of ~1 K is roughly consistent with *Wang et al.*'s [2012a] result for summer, although this study finds a greater increase for winter.

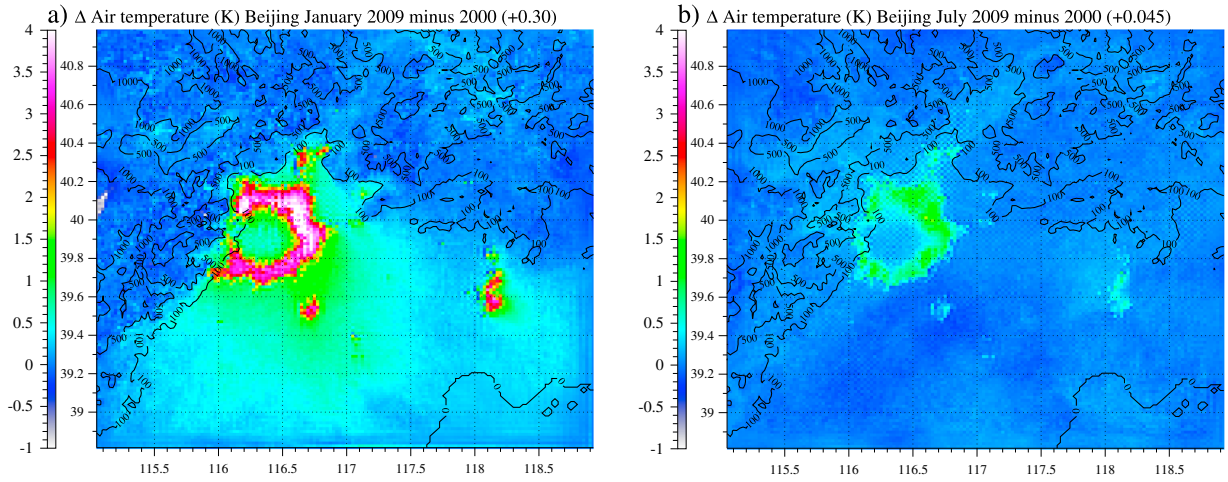

Figure 5. Same as Figure 2 but for near-surface air temperature.

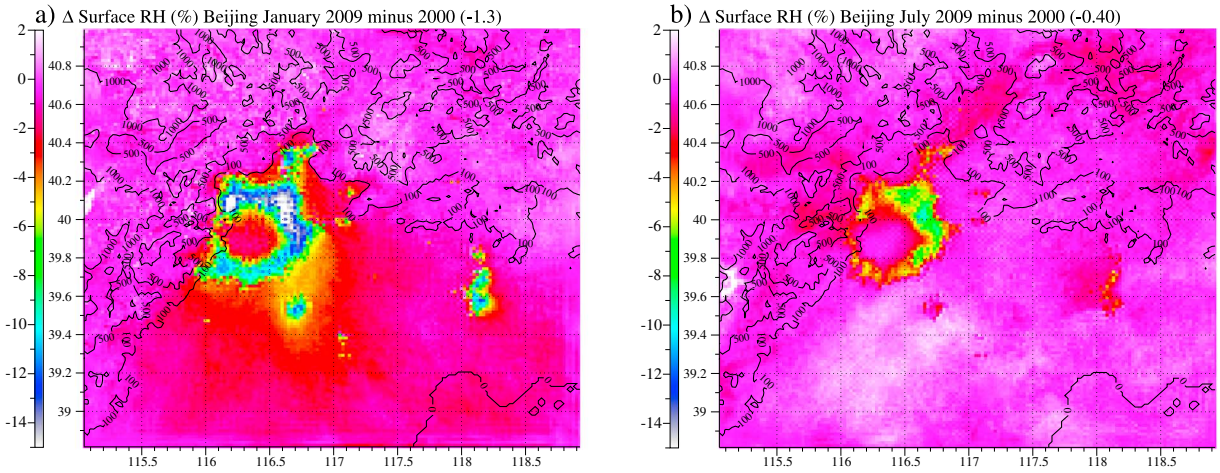

Figure 6. Same as Figure 2 but for near-surface relative humidity.

The increase in air temperatures and lesser evaporation of water due to urban surfaces decreases the near-surface relative humidity within the ring of impact (Figure 6). Decreases are roughly similar in January and July. The increase in surface roughness due to the new buildings reduces the near-surface wind speed there (Figure 7), with greater reductions in January because base wind speeds are higher in January. Reduced wind speeds increase wind shear and the resulting shearing stress by a peak of ~6 kg/m/s^2 in January and ~3 kg/m/s^2 in July. The greater air buoyancy due to the higher surface temperature combined with the greater shearing stress increases vertical turbulent kinetic energy (TKE) in the ring of impact (Figure 8), more in January than in July.

Higher TKE (Figure 8) increases vertical dilution, thereby decreasing the surface concentrations of many gas and particle pollutants, including total $PM_{2.5}$, NO_x, CO, NH_3, SO_2, and several organic gases. For example, the peak surface concentration decreases of $PM_{2.5}$ during both January and July are ~3 μg/m^3. Those of NO are ~5 ppbv in January and ~3 ppbv in July. The decreases in surface concentrations due to higher TKE are accompanied by increases aloft. Figure 9, for example, shows that particle number concentrations decrease near the surface but increase to a peak at ~300 m aloft in the zonal average in the ring of impact. Increases are greater in July than in January because of greater increases in TKE in January. Peak increases aloft exceed peak decreases at the surface in both months because urbanization also slows peak zonal wind speeds aloft more than at the surface (Figure 10), increasing air stagnation and reducing horizontal

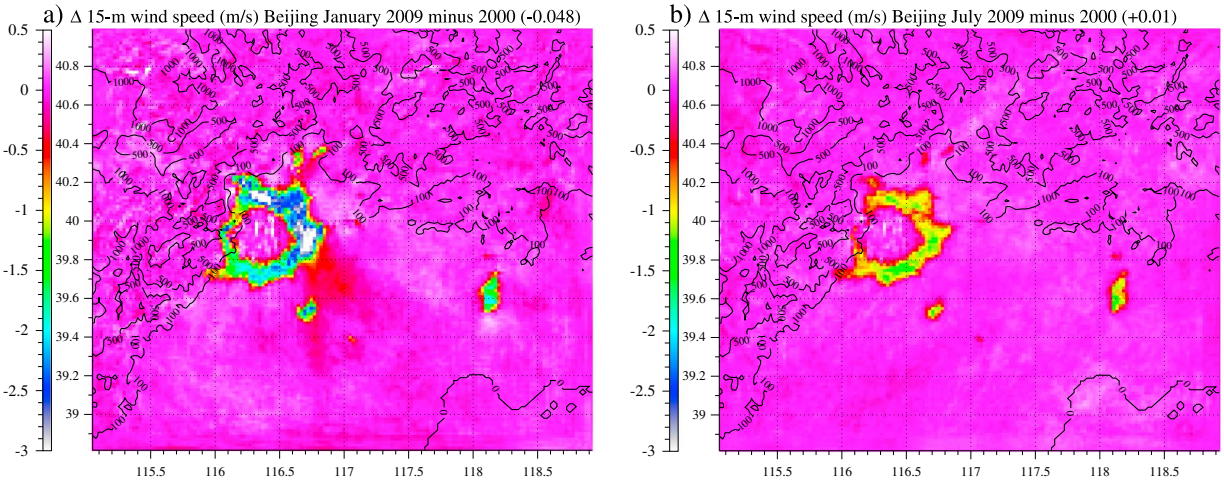

Figure 7. Same as Figure 2 but for near-surface wind speed.

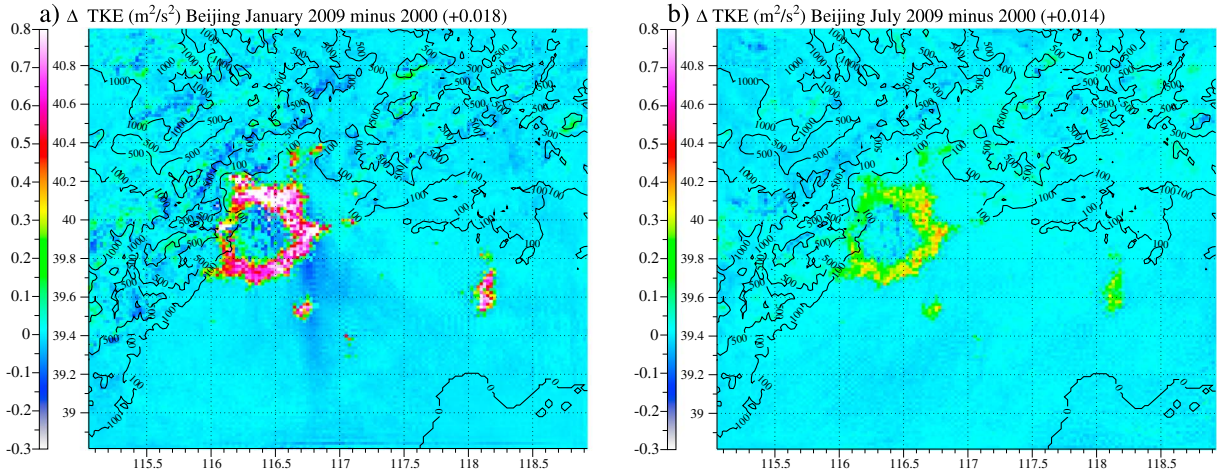

Figure 8. Same as Figure 2 but for near-surface turbulent kinetic energy.

pollutant transport aloft out of the megacity. As a result, total aerosol column loading and specific extinction increase over the ring of impact (Figure 11), Further, the higher number concentration of aerosol particles aloft increases cloud optical depth by a peak of 0.3 optical depth units in July but not much in January.

The reduction in near-surface NO, which is caused by enhanced TKE combined with higher near-surface air temperatures, increases ozone (Figure 12) and OH in the ring of impact. At high NO levels, NO titrates O_3, so decreases in NO increase O_3. *Jacobson* [2010] discusses the chemical basis for an increase in ozone with an increase in temperatures. Ozone changes are similar in January and July and occur mostly during the day. For example, the 24 h averaged peak increase in ozone in July is 1.8 ppbv (Figure 12), whereas the daytime-averaged peak increase is 2.1 ppbv in Beijing due to urbanization. The increase in ozone increases $O(^1D)$ by photolysis, and $O(^1D)$ reacted with H_2O to increase OH.

The simulations do not consider changes in anthropogenic emissions, so the changes are due solely to changes in meteorology, natural emission rates, and deposition rates caused by urbanization. For example, urbanization reduces leaf area, reducing emission surfaces for isoprene, monoterpenes, pollen, and spores from vegetation. At the same time, higher temperatures due to urbanization increase emission rates of gases from remaining vegetation in and around Beijing. The net effect in July is a small decrease in isoprene emissions due to urbanization of 0.018% summed over the model domain. However, pollen emissions, which are less temperature dependent, decline by ~0.32% due both to the reduction in vegetation and the reduction in wind speed in Beijing due to urbanization. The reduction in vegetation also reduces uptake of CO_2 and H_2O by photosyntheses.

Urbanization further encapsulates soils, reducing the ability of H_2, CH_4, NO, N_2O, H_2S, OCS, CS_2, and DMS produced by bacteria in soils to escape to the air in the model. However, higher soil temperatures in and around Beijing increase the rate of bacterial production of gases. For example, despite the lesser soil area available for NO emissions by soil bacteria, such emissions increase by ~0.22% in July, averaged over the

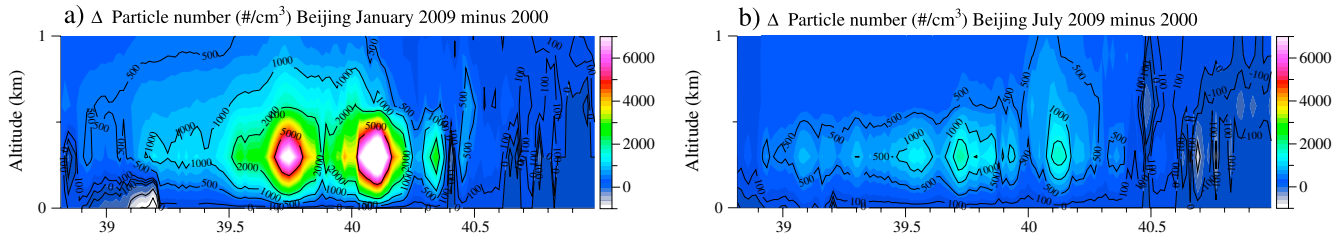

Figure 9. Same as Figure 2 but for zonally averaged aerosol particle number concentration. The lines are concentration contours.

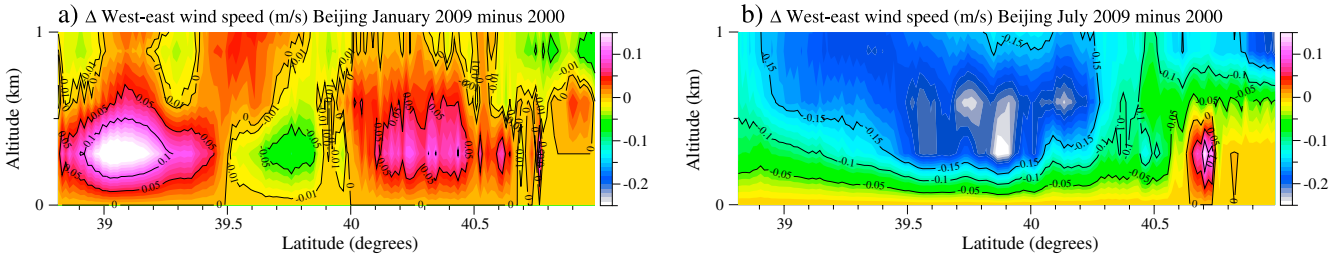

Figure 10. Same as Figure 9 but for zonally averaged west-east wind speed.

Beijing model domain, due to the higher temperatures. Soil methane emissions similarly increase by ~0.11% in July.

Encapsulation of soils also reduces bacterial uptake of H_2, CO, CH_4, NH_3, NO, HNO_3, and N_2O in soils in the model. Uptake of gases by bacteria is treated explicitly in the surface resistance term of the dry deposition speed in the model. The deposition speed also includes an aerodynamic resistance term that accounts for changes in TKE. Whereas encapsulating surfaces decreases gas metabolism by soil bacteria, urbanization increases TKE more over existing soil, causing a net increase in surface dry deposition speeds. For example, urbanization increases the H_2 dry deposition speed by a peak of 0.08 cm/s in January and 0.04 cm/s in July in the ring of impact.

Buildings replacing vegetated soil also increase surface roughness, feeding back to winds, turbulence, clouds, precipitation, and temperatures. For example, urbanization slightly increases precipitation over and downwind of Beijing by a maximum of 0.03 mm/d in January and 0.7 mm/d in July. This increase is consistent with studies that find increases in precipitation in or downwind of urban areas, generally due to enhanced convection from heating or changes in roughness due to urbanization [e.g., *Changnon*, 1981; *Jauregui and Romales*, 1996; *Bornstein and Lin*, 2000; *Niyogi et al*., 2006; *Shem and Shepherd*, 2009]. Changes in winds affect emission rates of not only pollen, spores, and bacteria but also of soil dust and sea spray. Changes in precipitation affect wet removal rates of all gases and particles.

Although this study is another step toward understanding better the impacts of urbanization on air quality and local weather and climate, it has some limitations. For example, it examines the short-term impacts for just 1 year, whereas urban areas are exposed to different climatological conditions over decades. Furthermore, changes in anthropogenic emissions, not treated here, have additional impacts on growing megacities. In addition, the road data developed, while more advanced than in many previous modeling studies, are still uncertain, as are rooftop and vegetation area data in urban megacities.

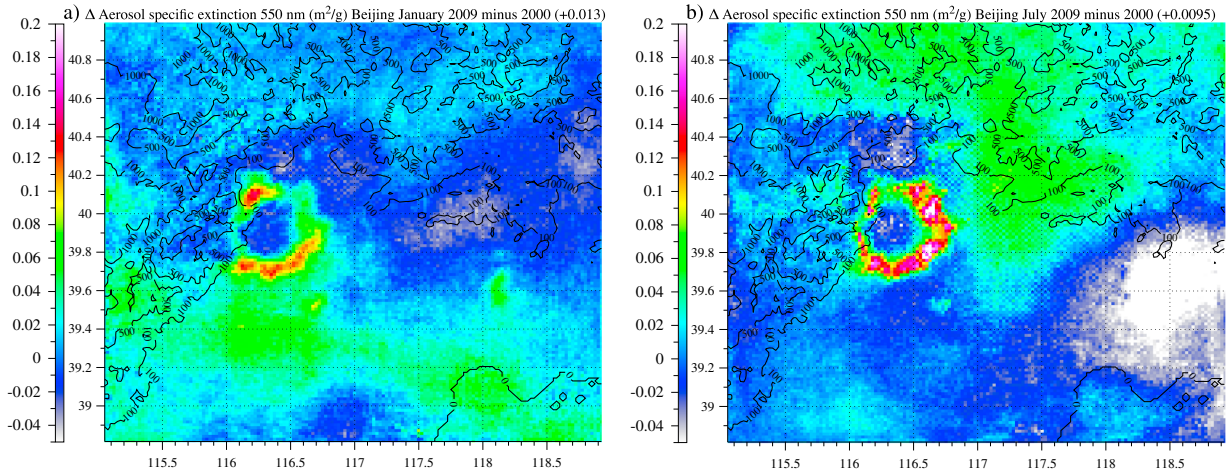

Figure 11. Same as Figure 2 but for 550 nm aerosol column specific extinction.

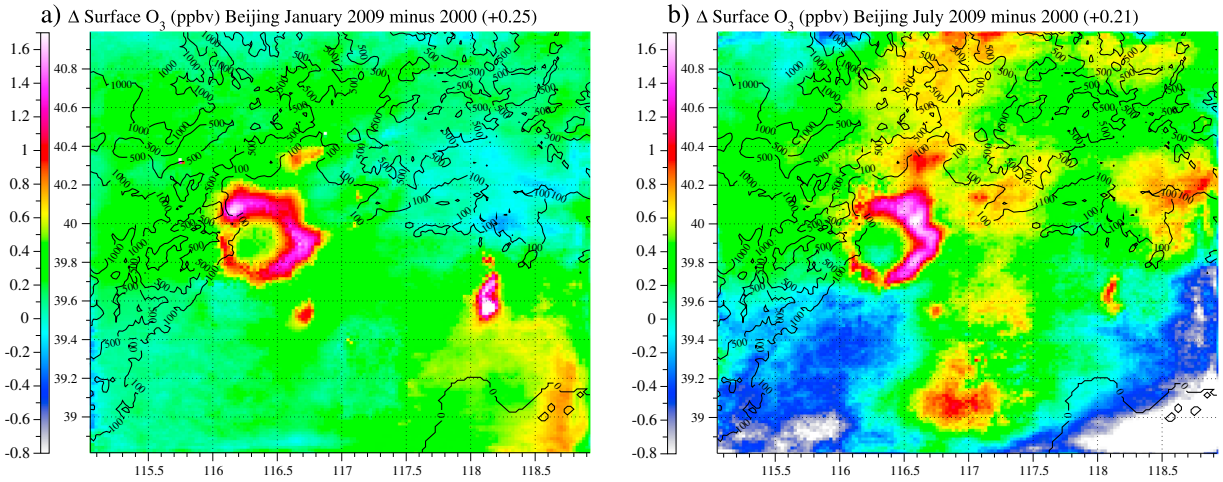

Figure 12. Same as Figure 2 but for near-surface ozone.

7. Summary and Conclusions

Simulations of the impacts of urbanization of Beijing's metropolitan extent between 2000 and 2009 were carried out. The simulations integrate new data sets for total urban extent and total road surface area and quantify the impacts of urbanization on several atmospheric parameters considering only differences in urban land uses and their physical properties. Results suggest that the urbanization of Beijing has created a ring of impact characterized by lowering surface albedo and soil moisture; increasing ground and air temperatures; increasing net downward surface solar radiation, shearing stress, and vertical turbulent kinetic energy; and decreasing the near-surface relative humidity and wind speed within the ring of impact. These simulations also found, in the absence of changes in anthropogenic emissions but accounting for changes in meteorologically driven natural emissions, that urbanization decreases the concentrations of many surface chemicals due to their vertical dilution but increases near-surface ozone, elevated pollution, and the total column of pollution above Beijing due to total-air stagnation. Furthermore, while encapsulation of soil due to urbanization reduces gas emissions from and uptake by bacteria in soil, higher temperatures due to urbanization increases the rate of metabolism and thus emissions by bacteria in nonencapsulated soils. Changes in wind speed, temperatures, and turbulence further compound the impacts of urbanization on natural gas and particle emissions and deposition speeds. Further work is needed to elucidate the combined impacts of anthropogenic emission changes together with urbanization on local air pollution and climate in changing megacities.

Acknowledgments

This project received funding from the NASA SMD Earth Sciences Division and computer support from the NASA high-end computing center. The research carried out at the Jet Propulsion Laboratory, California Institute of Technology, was supported under a contract with the National Aeronautics and Space Administration (NASA) Land-Cover and Land-Use Change (LCLUC) Program. The research carried out at the Department of Geography and Environment, University of Southampton, was done in the framework of the WorldPop Project (www.worldpop.org.uk) and supported by funding from the Bill & Melinda Gates Foundation (OPP1106427 and 1032350). Data used to generate figures and the table for this paper are available freely from the corresponding author at jacobson@stanford.edu.

References

Ackerman, T. P., and O. B. Toon (1981), Absorption of visible radiation in atmosphere containing mixtures of absorbing and nonabsorbing particles, *Appl. Optics*, *20*, 3661–3667.

Arakawa, A., and V. R. Lamb (1981), A potential enstrophy and energy conserving scheme for the shallow water equations, *Mon. Weather Rev.*, *109*, 18–36.

Bornstein, R. D., and Q. Lin (2000), Urban heat islands and summertime convective thunderstorms in Atlanta: Three case studies, *Atmos. Environ.*, *34*, 507–516.

Changnon, S. A., Jr. (1981), *METROMEX: A Review and Summary*, *Meteorol. Monogr.*, vol. 40, 181 pp., Am. Meteorol. Soc., Boston.

Chylek, P., V. Ramaswamy, and R. J. Cheng (1984), Effect of graphitic carbon on the albedo of clouds, *J. Atmos. Sci.*, *41*, 3076–3084.

Clarke, L., J. Edmonds, H. Jacoby, H. Pitcher, J. Reilly, and R. Richels (2007), Scenarios of greenhouse gas emissions and atmospheric concentrations, Sub-report 2.1A of Synthesis and Assessment Product 2.1 by the U.S. Climate Change Science Program and the Subcommittee on Global Change Research, 154 pp., Department of Energy, Office of Biological & Environmental Research, Washington, D. C. [Available at http://tntcat.iiasa.ac.at:8787/RcpDb/dsd?Action=htmlpage&page=compare, Accessed February 4, 2014.]

Dobson, J. E., E. A. Bright, P. R. Coleman, R. C. Durfee, and B. A. Worley (2000), LandScan: A global population database for estimating populations at risk, *Photogramm. Eng. Rem. Sens.*, *66*(7), 849–857.

European Commission Joint Research Centre/Netherlands Environmental Assessment Agency (PBL) (2014), Emission Database for Global Atmospheric Research (EDGAR). [Available at http://edgar.jrc.ec.europa.eu/datasets_grid_list42FT2010.php#d, Accessed March 4, 2014.]

Flanagin, A., and M. Metzger (2008), The credibility of volunteered geographic information, *GeoJournal*, *72*(3–4), 137–148, doi:10.1007/s10708-008-9188-y.

Global Forecast System (2013), 1° × 1° reanalysis fields. [Available at http://nomads.ncdc.noaa.gov/data/gfs-avn-hi/, Accessed September 14, 2013.]

Girres, J. F., and G. Touya (2010), Quality assessment of the French OpenStreetMap dataset, *Trans. GIS*, *14*, 435–459.

Goodchild, M. F. (2007), Citizens as sensors: The world of volunteered geography, *GeoJournal*, *69*(4), 211–221, doi:10.1007/s10708-007-9111-y.
Haklay, M. (2010), How good is OpenStreetMap information: A comparative study of OpenStreetMap and Ordnance Survey datasets for London and the rest of England, *Environ. Plann. B*, *37*, 682–703.
He, C., N. Okada, Q. Zhang, P. Shia, and J. Zhang (2006), Modeling urban expansion scenarios by coupling cellular automata model and system dynamic model in Beijing China, *Appl. Geogr.*, *26*, 323–345.
Howard, L. (1833), *The Climate of London*, vol. 1–3, W. Phillips, London.
International Organization for Standardization (2013), Data quality ISO19157:2013, International Organization for Standardization. [Available at http://www.iso.org/iso/home/store/catalogue_tc/catalogue_detail.htm?csnumber=32575, Accessed 7 November 2014.]
Jacobson, M. Z. (2001a), GATOR-GCMM: A global through urban scale air pollution and weather forecast model. 1. Model design and treatment of subgrid soil, vegetation, roads, rooftops, water, sea ice, and snow, *J. Geophys. Res.*, *106*, 5385–5402, doi:10.1029/2000JD900560.
Jacobson, M. Z. (2001b), GATOR-GCMM: 2. A study of day- and nighttime ozone layers aloft, ozone in national parks, and weather during the SARMAP Field Campaign, *J. Geophys. Res.*, *106*, 5403–5420, doi:10.1029/2000JD900559.
Jacobson, M. Z. (2002), Analysis of aerosol interactions with numerical techniques for solving coagulation, nucleation, condensation, dissolution, and reversible chemistry among multiple size distributions, *J. Geophys. Res.*, *107*(D19), 4366, doi:10.1029/2001JD002044.
Jacobson, M. Z. (2003), Development of mixed-phase clouds from multiple aerosol size distributions and the effect of the clouds on aerosol removal, *J. Geophys. Res.*, *108*(D8), 4245, doi:10.1029/2002JD002691.
Jacobson, M. Z. (2005a), A refined method of parameterizing absorption coefficients among multiple gases simultaneously from line-by-line data, *J. Atmos. Sci.*, *62*, 506–517.
Jacobson, M. Z. (2005b), Studying ocean acidification with conservative, stable numerical schemes for nonequilibrium air-ocean exchange and ocean equilibrium chemistry, *J. Geophys. Res.*, *110*, D07302, doi:10.1029/2004JD005220.
Jacobson, M. Z. (2010), The enhancement of local air pollution by urban CO_2 domes, *Environ. Sci. Technol.*, *44*, 2497–2502, doi:10.1021/es903018m.
Jacobson, M. Z. (2012), Investigating cloud absorption effects: Global absorption properties of black carbon, tar balls, and soil dust in clouds and aerosols, *J. Geophys. Res.*, *117*, D06205, doi:10.1029/2011JD017218.
Jacobson, M. Z., and D. G. Streets (2009), The influence of future anthropogenic emissions on climate, natural emissions, and air quality, *J. Geophys. Res.*, *114*, D08118, doi:10.1029/2008JD011476.
Jacobson, M. Z., and J. E. Ten Hoeve (2012), Effects of urban surfaces and white roofs on global and regional climate, *J. Clim.*, *25*, 1028–1044, doi:10.1175/JCLI-D-11-00032.1.
Jacobson, M. Z., Y. J. Kaufmann, and Y. Rudich (2007), Examining feedbacks of aerosols to urban climate with a model that treats 3-D clouds with aerosol inclusions, *J. Geophys. Res.*, *112*, D24205, doi:10.1029/2007JD008922.
Jauregui, E., and E. Romales (1996), Urban effects on convective precipitation in Mexico City, *Atmos. Environ.*, *30*, 3383–3389.
Jones, P. D., P. Ya, M. Groisman, M. Coughlan, N. Plummer, W. C. Wang, and T. R. Karl (1990), Assessment of urbanization effects in time series of surface air temperature over land, *Nature*, *347*, 169–172.
Ketefian, G. S., and M. Z. Jacobson (2009), A mass, energy, vorticity, and potential enstrophy conserving boundary treatment scheme for the shallow water equations, *J. Comp. Phys.*, *228*, 1–32, doi:10.1016/j.jcp.2008.08.009.
Koukoletsos, T., M. Haklay, and C. Ellul (2012), Assessing data completeness of VGI through an automated matching procedure for linear data, *Trans. GIS*, *16*, 477–498.
Kressler, F., and K. Steinnocher (1996), Change detection in urban areas using satellite data and spectral mixture analysis, *Int. Arch. Photogram. Rem. Sens.*, *31*, 379–383.
Kuang, W., Y. Dou, C. Zhang, W. Chi, A. Liu, Y. Liu, R. Zhang, and J. Liu (2015), Quantifying the heat flux regulation of metropolitan land use/land cover components by coupling remote sensing modeling with in situ measurement, *J. Geophys. Res. Atmos.*, *120*, 113–130, doi:10.1002/2014JD022249.
Li, C. C., J. Wang, L. Wang, L. Y. Hu, and P. Gong (2014), Comparison of classification algorithms and training sample sizes in urban land classification with Landsat Thematic Mapper imagery, *Rem. Sens.*, *6*, 964–983.
Lu, R., and R. P. Turco (1995), Air pollutant transport in a coastal environment: II. Three-dimensional simulations over Los Angeles basin, *Atmos. Environ.*, *29*, 1499–1518.
Mellor, G. L., and T. Yamada (1982), Development of a turbulence closure model for geophysical fluid problems, *Rev. Geophys. Space Phys.*, *20*, 851–873.
Moderate Resolution Imaging Spectroradiometer/USGS (2007), Terra plus Aqua Combined Albedo 16-Day L3 Global 0.05° CMG V4 data. [Available at https://lpdaac.usgs.gov/lpdaac/products/modis_products_table/brdf_albedo_model_parameters/16_day_l3_0_05deg_cmg/mcd43c1, Accessed 2007.]
Nakayama, Y., K. I. Ohshima, and Y. Fukamachi (2012), Enhancement of sea ice drift due to the dynamical interaction between sea ice and a coastal ocean, *J. Phys. Oceanogr.*, *42*, 179–192.
Neis, P., and D. Zielstra (2014), Recent developments and future trends in volunteered geographic information research: The case of OpenStreetMap, *Future Internet*, *6*, 76–106, doi:10.3390/fi6010076.
Neis, P., M. Goetz, and A. Zipf (2012a), Towards automatic vandalism detection in OpenStreetMap, *ISPRS Int. J. Geo-Inf.*, *1*, 315–332.
Neis, P., D. Zielstra, and A. Zipf (2012b), The street network evolution of crowd-sourced maps: OpenStreetMap in Germany 2007–2011, *Future Internet*, *4*, 1–21.
Nghiem, S. V., D. Balk, E. Rodriguez, G. Neumann, A. Sorichetta, C. Small, and C. D. Elvidge (2009), Observations of urban and suburban environments with global satellite scatterometer data, *ISPRS J. Photogram. Rem. Sens.*, *64*, 367–380, doi:10.1016/j.isprsjprs.2009.01.004.
Nghiem, S. V., A. Sorichetta, C. D. Elvidge, C. Small, D. Balk, U. Deichmann, and G. Neumann (2014), Remote sensing of urban environments—The Beijing case study, in *Encyclopedia of Remote Sensing*, edited by E. Njoku, pp. 869–878, Springer, New York, Heidelberg, Dordrecht, London.
Niyogi, D., T. Holt, S. Zhong, P. C. Pyle, and J. Basara (2006), Urban and land surface effects on the 30 July 2003 mesoscale convective system event observed in the southern Great Plains, *J. Geophys. Res.*, *111*, D19107, doi:10.1029/2005JD006746.
Oke, T. R. (1982), The energetic basis of the urban heat island, *Q. J. R. Meteorol. Soc.*, *108*, 1–24.
Oleson, K. W., G. B. Bonan, J. Feddema, and T. Jackson (2011), An examination of urban heat island characteristics in a global climate model, *Int. J. Climatol.*, *31*(12), 1848–1865, doi:10.1002/joc.220.
Peterson, T. C. (2003), Assessment of urban versus rural in situ surface temperatures in the contiguous United States: No difference found, *J. Clim.*, *16*, 2941–2959.
Pon, B. (1999), Pavement albedo, heat island group. [Available at http://heatisland.lbl.gov/Pavements/Albedo/.]
QuikSCAT Mission (2014), Jet Propulsion Laboratory, California Institute of Technology. [Available at https://winds.jpl.nasa.gov/missions/quikscat/, Accessed September 2, 2014.]

Santini, M., A. Taramelli, and A. Sorichetta (2010), ASPHAA: A GIS-based algorithm to calculate cell area on a latitude-longitude (geographic) regular grid, *Trans. GIS*, *14*(3), 351–377, doi:10.1111/j.1467-9671.2010.01200.x.

Sarrat, C., A. Lemonsu, V. Masson, and D. Guedalla (2006), Impact of urban heat island on regional atmospheric pollution, *Atmos. Environ.*, *40*, 1743–1758.

Schaaf, C., et al. (2002), First operational BRDF, albedo nadir reflectance products from MODIS, *Remote Sens. Environ.*, *83*, 135–148.

Shem, W., and M. Shepherd (2009), On the impact of urbanization on summertime thunderstorms in Atlanta: Two numerical model case studies, *Atmos. Res.*, *92*, 172–189.

Small, C. (2005), A global analysis of urban reflectance, *Int. J. Rem. Sens.*, *26*, 661–681.

Song, W., and G. Sun (2010), The role of mobile volunteered geographic information in urban management, in *18th International Conference on Geoinformatics*, edited by Y. Liu and A. Chen, pp. 1–5, Liaoning Tech. Univ., Fuxin, China.

Song, X., J. Zhang, A. AghaKouchak, S. Sen Roy, Y. Xuan, G. Wang, R. He, X. Wang, and C. Liu (2014), Rapid urbanization and changes in spatiotemporal characteristics of precipitation in Beijing metropolitan area, *J. Geophys. Res. Atmos.*, *119*, 11,250–11,271, doi:10.1002/2014JD022084.

Sorichetta, A., S. V. Nghiem, M. Masetti, A. Richter, C. Linard, A. E. Gaughan, F. R. Stevens, and A. J. Tatem (2014), China mega-urbanization in the 2000s and its environmental impact, paper presented at Urbanization and Development in China, Univ. of Southampton, U. K., 30 - 31 Oct.

Stevenazzi, S., M. Masetti, S. V. Nghiem, and A. Sorichetta (2015), Groundwater vulnerability maps derived from time dependent method using satellite scatterometer data, *Hydrogeol. J.*, *23*, 631–647, doi:10.1007/s10040-015-1236-3.

Toon, O. B., C. P. McKay, T. P. Ackerman, and K. Santhanam (1989), Rapid calculation of radiative heating rates and photodissociation rates in inhomogeneous multiple scattering atmospheres, *J. Geophys. Res.*, *94*, 16,287–16,301, doi:10.1029/JD094iD13p16287.

United Nations, Department of Economic and Social Affairs, Population Division (2014), World Urbanization Prospects: The 2014 Revision, Highlights (ST/ESA/SER.*A*/352), United Nations, New York.

United States Geological Survey (USGS) (2006), Land cover type yearly L3 global 500 m V5 data, processed to 0.01°. [Available at https://lpdaac.usgs.gov/.]

Velazquez-Lozada, A., J. E. Gonzalez, and A. Winter (2005), Urban heat island effect analysis for San Juan, Puerto Rico, *Atmos. Environ.*, *40*, 1731–1741.

Walcek, C. J. (2000), Minor flux adjustment near mixing ratio extremes for simplified yet highly accurate monotonic calculation of tracer advection, *J. Geophys. Res.*, *105*(D7), 9335–9348, doi:10.1029/1999JD901142.

Wang, J., J. Feng, Z. Yan, Y. Hu, and J. Gia (2012a), Nested high-resolution modeling of the impact of urbanization on regional climate in three vast urban agglomerations in China, *J. Geophys. Res.*, *117*, D21103, doi:10.1029/2012JD018226.

Wang, L., et al. (2012b), China's urban expansion from 1990 to 2010 determined with satellite remote sensing, *Chinese Sci. Bull.*, *57*(22), 2802–2812, doi:10.1007/s11434-012-5235-7.

Wang, M., Q. Li, Q. Hu, and M. Zhou (2013), Quality analysis of Open Street Map data, paper presented at the 8th International Symposium on Spatial Data Quality, Hong Kong, China.

Weng, Q., X. Hu, and H. Liu (2009), Estimating impervious surfaces using linear spectral mixture analysis with multitemporal ASTER images, *Int. J. Rem. Sens.*, *30*, 4807–4830.

Wikipedia (2014), Geography of Beijing. [Available at http://en.wikipedia.org/wiki/Geography_of_Beijing, Accessed September 25, 2013.]

Will, J. (2014), Development of an automated matching algorithm to assess the quality of the OpenStreetMap road network—A case study in Göteborg, Sweden, M.S. thesis, Department of Physical Geography and Ecosystem Science, Lund University.

World Bank and the Development Research Center of the State Council, P. R. China (2014), *Urban China: Toward Efficient, Inclusive, and Sustainable Urbanization*, World Bank, Washington, D. C.

Xie, Y., C. Fang, G. C. S. Lin, H. Gong, and B. Qiao (2007), Tempo-spatial patterns of land use changes and urban development in globalizing China: A study of Beijing, *Sensors*, *7*, 2881–2096.

Yang, L., F. Tian, J. A. Smith, et al. (2014), Urban signatures in the spatial clustering of summer heavy rainfall events over the Beijing metropolitan region, *J. Geophys. Res. Atmos.*, *119*, 1203–1217, doi:10.1002/2013JD020762.

Zhang, C. L., F. Chen, S. G. Miao, Q. C. Li, X. A. Xia, and C. Y. Xuan (2009), Impacts of urban expansion and future green planting on summer precipitation in the Beijing metropolitan area, *J. Geophys. Res.*, *114*, D02116, doi:10.1029/2008JD010328.

Zhang, Q., C. Schaaf, and K. C. Seto (2013), The vegetation adjusted NTL urban index: A new approach to reduce saturation and increase variation in nighttime luminosity, *Remote Sens. Environ.*, *129*, 32–41.

Zheng S. D., and J. H. Zheng (2014), Assessing the completeness and positional accuracy of OpenStreetMap in China, in *Thematic Cartography for the Society, Lecture, Notes in Geoinformation and Cartography*, edited by T. Bandrova, et al., Springer International, Switzerland, doi:10.1007/978-3-319-08180-9_14.

Zielstra, D., and H. H. Hochmair (2011), A comparative study of pedestrian accessibility to transit stations using free and proprietary network data, *Transp. Res. Rec. J. Transp. Res. Board*, *2217*, 145–152.

Zielstra, D., and A. Zipf (2010), A comparative study of proprietary geodata and volunteered geographic information for Germany, paper presented at the 13th AGILE international conference on geographic information science, Guimarães, Portugal.

Zielstra, D., H. H. Hochmair, and P. Neis (2013), Assessing the effect of data imports on the completeness of OpenStreetMap—A United States case study, *Trans. GIS*, *17*, 315–334.